

White Dwarfs with Infrared Excess in the HET Dark Energy Experiment

RUDY A. MORALES,¹ BARBARA G. CASTANHEIRA,¹ JAYDEN BLANCHARD,¹ DETLEV KOESTER,² PÉTER NÉMETH,³ S. O. KEPLER,⁴ ERIN MENTUCH COOPER,^{5,6} AND KARL GEBHARDT⁷

¹Department of Physics and Astronomy, Baylor University, Waco, TX 76798-7316, U.S.A.

²Institut für Theoretische Physik und Astrophysik, University of Kiel, 24098 Kiel, Germany

³Astroserver.org, Fő tér 1, 8533 Malomcsok, Hungary

⁴Instituto de Física, Universidade Federal do Rio Grande do Sul, 91501-970 Porto Alegre, Brazil

⁵Department of Astronomy, The University of Texas at Austin, 2515 Speedway Boulevard, Austin, TX 78712, USA

⁶McDonald Observatory, The University of Texas at Austin, 2515 Speedway Boulevard, Austin, TX 78712, USA

⁷Department of Astronomy, The University of Texas at Austin, 2515 Speedway Boulevard, Stop C1400, Austin, TX 78712, USA

ABSTRACT

White dwarfs with infrared excess emission provide a window into the late stages of stellar evolution and the dynamics of circumstellar environments. Using data from the Hobby-Eberly Telescope Dark Energy Experiment (HETDEX), we characterized 30 white dwarfs exhibiting infrared excess, including 29 DA and 1 DB stars. While an infrared excess can arise from dusty disks or cool (sub-)stellar companions, our sample is limited to stellar companions due to our selection based on SDSS photometry, which is sensitive to excess emission at wavelengths $\lambda < 1 \mu\text{m}$. Our sample contains 22 newly identified excess sources not previously reported in the literature. Spectroscopic observations are available for 10 sources via SDSS, of which only 8 have prior spectroscopic classifications in the literature.

In this paper, we present the determination of the effective temperature and surface gravity of these white dwarfs. We used the Balmer line profiles to compare with current atmospheric models to determine the photospheric parameters of the white dwarfs, minimizing contamination introduced by the infrared source. We used photometric data from the SDSS and the *Gaia* mission to resolve the degeneracies between hot and cold solutions from spectroscopy, constraining the photospheric parameters. These results help refine our understanding of white dwarf evolution in binary systems, focusing on stellar companions that cause the infrared excess.

This study contributes to identifying systems with potential substellar companions or unresolved stellar partners, adding to the growing effort to map out the fate of planetary systems after their host stars evolve beyond the main sequence.

Keywords: White Dwarf Stars — Infrared Excess — Balmer line profiles — Atmospheric models — HETDEX Survey

1. INTRODUCTION

White dwarfs (WDs) represent the endpoint in stellar evolution for the vast majority of single stars (e.g. Winget & Kepler 2008), with a wide range of progenitor masses from $0.08 M_{\odot}$ to $8-10.5 M_{\odot}$ (e.g. Woosley & Heger 2015). They provide a fundamental constraint for our understanding of stellar evolution and binary interaction. White dwarfs with infrared (IR) excess offer a unique opportunity to study the circumstellar environments of evolved stars and probe the final stages of planetary system evolution. These systems are also exciting targets for follow-up with facilities like JWST, which can spectroscopically characterize planetary debris and detect low-mass companions at mid-infrared wavelengths, as demonstrated by recent discoveries (e.g., Mullally et al. 2024; Farihi et al. 2025). Our results add new candidates to the growing population of white dwarfs with infrared excess associated with unresolved stellar or substellar companions. Numerous studies have explored this phenomenon using data from WISE and other IR surveys (Xu et al. 2020; Lai et al. 2021), re-

vealing that a significant fraction of WDs particularly those with low-mass companions—exhibit detectable excess emission at IR wavelengths.

When in binary systems — both interacting and non-interacting — white dwarfs may be the progenitors of a variety of interesting systems, including AM CVn systems, cataclysmic variables, and perhaps most interestingly, type Ia supernovae (SNe Ia) (Iben & Tutukov 1994). When the companion to the white dwarf evolves into a giant or supergiant, mass transfer through Roche lobe overflow can lead to nova outbursts or, if the white dwarf nears the Chandrasekhar limit, a thermonuclear explosion. Alternatively, the double-degenerate channel involves two white dwarfs and may also produce SNe Ia (Livio & Pringle 2011). These phenomena underscore the importance of white dwarfs for understanding stellar remnants, binary evolution, and explosive transients.

Infrared excess in white dwarfs is a powerful diagnostic of their surrounding environments and late-stage planetary system evolution. This excess emission can arise from one of three primary sources: a dusty circumstellar disk formed from tidally disrupted planetary bodies, a cool brown dwarf companion, or a low-mass main-sequence star such as an M dwarf (Rebassa-Mansergas et al. 2019). Recent studies suggest that dusty disks are detected in approximately 2–4% of white dwarfs (Barber et al. 2014; Rocchetto et al. 2015; Wilson et al. 2019; Rebassa-Mansergas et al. 2019), while brown dwarf companions account for about 0.5–2.0% (Lai et al. 2021 and references therein). M-dwarf companions occur in about 28% of systems (Debes et al. 2011). Identifying the nature of the excess is crucial for understanding white dwarf binarity, planetary debris, and accretion processes.

A particularly well-studied case is G29-38, a pulsating white dwarf (Shulov & Kopatskaya 1974) that also shows a significant infrared excess. Initially, Zuckerman & Becklin (1987) proposed that the excess was due to a brown dwarf or planetary companion, but follow-up observations revealed a dusty disk composed primarily of amorphous olivine and a small amount of forsterite, located within $1\text{--}5 R_{\odot}$ of the white dwarf (Reach et al. 2005). More recently, Cunningham et al. (2022) used X-ray observations to infer an active accretion rate of planetary debris onto the white dwarf. This system exemplifies the kind of complex circumstellar environments that can be revealed through multiwavelength studies of infrared excess.

Using newly available spectra from HETDEX, in combination with complementary photometric and astrometric data from SDSS, *Gaia*, 2MASS, and WISE, we analyzed a sample of 30 white dwarfs exhibiting in-

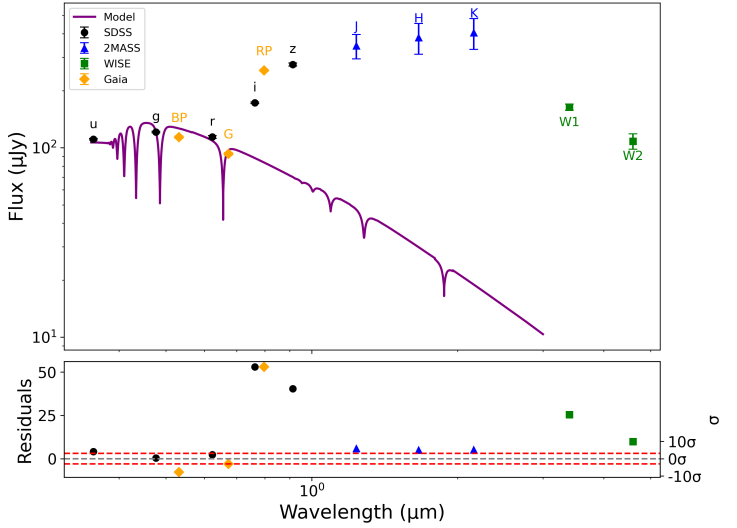


Figure 1. Top Panel: Spectral energy distribution (SED) fitting for the white dwarf SDSSJ113907.57+511103.6. The best-fit DA white dwarf model (purple) is compared to optical photometry from u , g , r , i , z (black) and G , BP , RP (orange diamonds). While the model closely matches the u , g , r bands, significant deviations are present at i , z and RP (high outliers), as well as BP and G (low outliers). An IR excess is detected at J (blue) just above 3σ and $W1$, $W2$ (green) bands. **Bottom Panel:** Residuals expressed in units of measurement uncertainty (σ), with red dashed lines indicating the $\pm 3\sigma$ threshold for identifying significant excess or deficit in the observed flux.

frared excess to determine their atmospheric parameters. For most of our targets, these HETDEX spectra represent their first spectroscopic measurements, providing a unique opportunity to characterize systems that have previously lacked detailed spectral analysis. In this paper, we describe the spectroscopic analysis of the HETDEX data, combined with all publicly available data from other surveys, such as the Sloan Digital Sky Survey (Kleinman et al. 2004; Kepler et al. 2021) and the *Gaia* mission (Gentile Fusillo et al. 2021). We discuss the fitting methods and the best determinations for the photospheric parameters of the white dwarfs.

2. DATA

2.1. Sample Selection and HETDEX

The primary goal of this study is to identify and characterize WDs with infrared (IR) excess signatures using spectroscopic and photometric data. This project is based on sources identified in the HETDEX survey (Hill et al. 2006; Adams et al. 2011; Gebhardt et al. 2021), which aims to probe dark energy by measuring the Hubble parameter, $H(z)$, and the angular diame-

ter distance, $D_A(z)$, to explore the potential evolution of dark energy density (Gebhardt et al. 2021). This is achieved by observing a large number of Lyman- α emitting galaxies with redshifts between $1.9 \leq z \leq 3.5$ across approximately ~ 450 deg 2 of the northern sky. HETDEX utilizes the Visible Integral Field Replicable Unit Spectrograph (VIRUS; Hill et al. 2021), composed of 156 low-resolution ($R \sim 750$) spectrographs covering the wavelength range 3500–5500 Å, with a field of view of 22 arcmin, a segmented 11 m primary mirror, and 35,000 fibers in 78 integral field units. Each fiber is separated by 2.5", with a diameter of 1.5". To ensure comprehensive flux sampling from all observing targets, the survey performs three dithered pointings of 6 minutes each.

Although HETDEX was not initially designed for stellar science, its magnitude-limited nature ensures that all continuum sources falling within the fibers are recorded. The Hobby-Eberly Telescope (HET) VIRUS Parallel Survey (HETVIPS) has reduced and made available to the community a continuum source catalog based on HETDEX observations (Zeimann et al. 2024).

To identify white dwarfs within the HETDEX continuum catalog, we performed a positional cross-match with white dwarf catalogs from the Sloan Digital Sky Survey (SDSS; Kleinman et al. 2004; Kepler et al. 2024) and Gaia DR3 (Gentile Fusillo et al. 2021). The cross-match used sky coordinates (Right Ascension and Declination) with a maximum angular separation of 2 arcseconds to ensure accurate identification. This initial sample consisted of approximately 200 white dwarfs. No strict magnitude limits or quality cuts (e.g., photometric errors, parallax uncertainties, or astrometric flags) were applied at this stage; instead, the goal was to create a broad sample of WDs.

2.2. Identifying IR Excess White dwarfs

To confirm the presence of IR excess and ensure it was not an artifact of flux calibration or photometric uncertainties, we performed spectral energy distribution (SED) fitting using available optical and infrared photometry, following approaches in e.g., Tremblay & Bergeron (2007) and Girven et al. (2011). Starting from an initial sample of approximately 200 white dwarfs identified as described above, we cross-matched these sources with the Two Micron All Sky Survey (2MASS; Skrutskie et al. 2006) and the CatWISE catalog (Eisenhardt et al. 2020; Marocco et al. 2021), which was constructed using data from the Wide-field Infrared Survey Explorer (WISE; Wright et al. 2010) and its extension NEOWISE (Mainzer et al. 2011), to obtain near- and mid-infrared fluxes. Cross-matching was performed using sky coordi-

nates with a maximum angular separation of 2 arcseconds to ensure reliable associations.

To assess potential IR excess, we examined color-color diagrams (e.g., $u - g$, $g - r$, $r - i$, and $BP - RP$) and flagged sources that appeared redder than canonical white dwarf sequences. In addition, we considered SDSS targets flagged for red or IR excess, as these could indicate the presence of unresolved stellar or substellar companions, such as low-mass stars or brown dwarfs. Our analysis focuses on identifying such companions, as circumstellar dust or debris disks cannot be reliably detected in the optical bands ($\lambda < 1 \mu\text{m}$) used in our selection.

Table 1 summarizes the photometric properties of these objects, indicates which targets have been previously reported in the literature, and identifies those for which the first spectroscopic observation was obtained through HETDEX.

For each object, we constructed an SED using SDSS ($ugriz$), Gaia (G , BP , RP), 2MASS (JHK_s), and WISE ($W1-W2$) photometry where available. Each SED was fitted with a white dwarf atmospheric model anchored on the optical data. An IR excess was flagged only when at least one 2MASS or WISE $W1$ or $W2$ photometric point exceeded the model prediction by more than 3σ , taking into account photometric uncertainties. The $W3$ and $W4$ bands were excluded from the IR excess selection criteria due to their broader point spread functions and lower sensitivity, which increase the likelihood of background contamination or source confusion

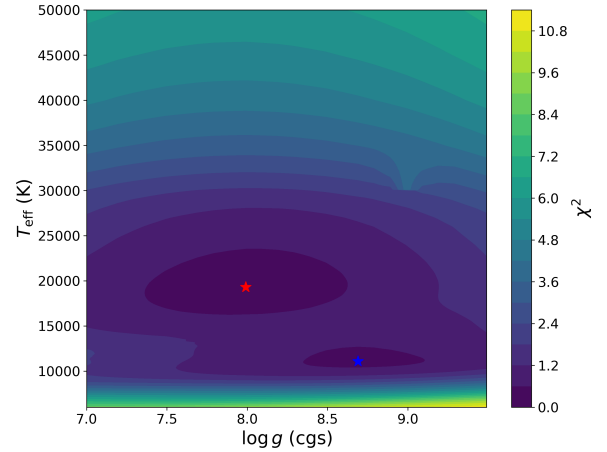


Figure 2. Contour plot of the S values computed by comparing all the DA models in our grid to the observed spectrum of the star SDSS J113907.57+511103.6. The red star represents the “hot” solution, while the blue star corresponds to the “cold” solution, reflecting the degeneracy in the Balmer lines fitting technique.

(Debes et al. 2011; Dennihy et al. 2020). This filtering reduced the sample to 30 white dwarfs with statistically significant IR excess.

Figure 1 illustrates this method using the example of SDSSJ113907.57+511103.6. The optical photometry from SDSS and Gaia generally aligns with the white dwarf model; however, elevated fluxes in SDSS i , z , and Gaia RP suggest the possible presence of a low-mass companion, such as an M dwarf, contributing red excess. In the infrared, the 2MASS J band lies just above the 3σ detection threshold, while WISE $W1$ and $W2$ show clear and significant excess relative to the model, consistent with an infrared excess. The bottom panel of Figure 1 presents the residuals between the observed photometry and the white dwarf model, highlighting significant deviations at longer wavelengths consistent with the presence of IR-emitting sources, in our case being stellar companions.

Although our analysis excluded $W3$ and $W4$ from the selection criteria, it is important to interpret WISE-based excesses with caution. As shown by Dennihy et al. (2020), IR excess detections from WISE—particularly for faint white dwarfs—can include false positives even after standard vetting procedures such as astrometric filtering and high-resolution imaging. No objects in our sample were flagged based on $W3$ or $W4$, as most sources are undetected or have only upper limits in these bands. We plan to obtain higher-resolution follow-up observations in the near- and mid-infrared (1.0–5.0 μm) using instruments such as the Gemini/GNIRS high-resolution IFU ($R \sim 1200$ –19000) to further investigate the nature of the IR excesses.

3. SPECTROSCOPIC ANALYSIS

In this section, we describe our comparison of the HETDEX spectra for the white dwarfs identified in the continuum catalog that have infrared excess to atmospheric models. To accomplish the goals of HETDEX, the observations of Lyman- α emitting galaxies must be very accurately flux calibrated, which is not a trivial task in a telescope like the HET, with a fixed altitude, where the effective aperture of the mirror changes during the observations. Gebhardt et al. (2021) discussed in detail their approach to model the throughput for HETDEX observations, testing their method by comparing the fluxes of various stars within their survey and SDSS spectra (see their Figure 16). Data from all sources observed by HETDEX have been systematically reduced by the HETDEX team (Ziemann et al. 2024), which includes flux calibration of the continuum sources.

Although we benefit from spectra with well-calibrated flux, our initial fitting strategy focused exclusively on

the normalized spectral lines rather than the full fluxed spectrum. This is consistent with our focus on probing stellar companions, which are the primary interpretation for the IR excesses in our sample. These secondary components can contribute significantly to the continuum level but do not typically affect the hydrogen or helium line profiles that are used to determine the white dwarf’s photospheric parameters. Thus, by isolating and fitting only the hydrogen or helium lines, we ensure that the derived values of T_{eff} and $\log g$ reflect the intrinsic properties of the white dwarf atmosphere.

3.1. Models

We have used an updated model grid based on the LTE atmospheric models described in Koester (2010) to determine the effective temperature (T_{eff}) and surface gravity ($\log g$) for white dwarfs with infrared excess. These models have been refined in subsequent works through improvements in the input physics, including updated Stark broadening profiles for hydrogen lines, improved treatment of convective energy transport using the $\text{ML2}/\alpha = 0.8$ prescription (a mixing-length theory formulation where "ML2" refers to a specific choice of convective efficiency parameters and α is the mixing length to pressure scale height ratio), and more accurate opacities and equation-of-state treatments (e.g., Koester & Kepler 2019; Koester et al. 2020).

The grid of DA models spans $6,000 \text{ K} \leq T_{\text{eff}} \leq 50,000 \text{ K}$ and $7 \leq \log g \leq 9.5$ (cgs units), and was calculated for $\text{ML2}/\alpha = 0.8$. The grid of DB models is slightly different, ranging from $3,000 \text{ K} \leq T_{\text{eff}} \leq 70,000 \text{ K}$, $7 \leq \log g \leq 9.5$ (cgs units), and relative abundances of hydrogen $-9 \leq \log \text{H/He} \leq 0$. In our sample, all stars have spectral type DA, except for one DB (discussed in Section 3.3).

3.2. Fitting DA White Dwarfs

HETDEX observations cover a fixed wavelength range that includes the Balmer series from $\text{H}\beta$ to $\text{H}\eta$. While $\text{H}\eta$ is technically within this range, we exclude it from our fitting due to the combination of reduced line strength at higher-order transitions and increased sensitivity (Kepler et al. 2006) to theoretical uncertainties in line broadening at these wavelengths. This approach follows established spectroscopic techniques that limit fitting to $\text{H}\beta$ through $\text{H}\zeta$ to ensure robust and consistent parameter determination (Bergeron et al. 1992; Liebert et al. 2005; Gianninas et al. 2011; Tremblay et al. 2011, 2013).

Our spectroscopic analysis begins by centering each Balmer line to ensure the isolation of the line profiles. Proper centering is essential to minimize systematic er-

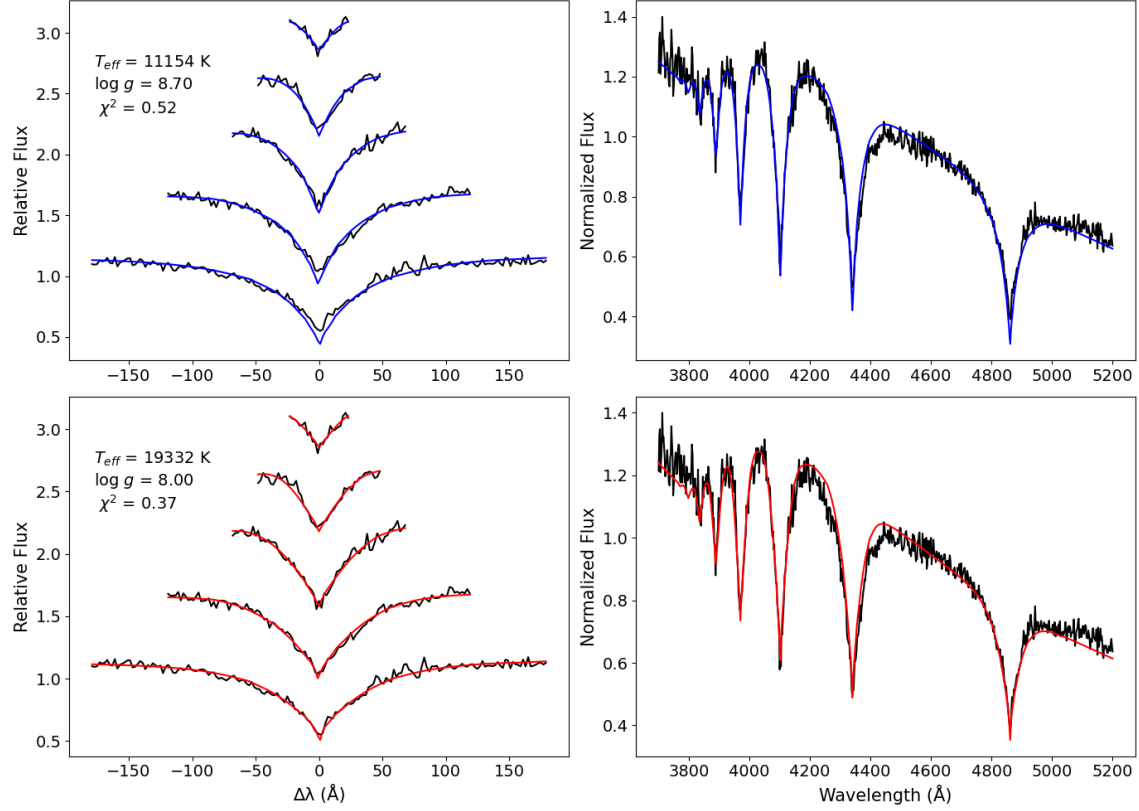


Figure 3. Example of our DA fitting procedure for SDSS J113907.57+511103.6. **Top Left Panel:** Best “cold” solution for Balmer line fitting, observed Balmer line profiles (black) and best model (blue) with $T_{\text{eff}} = 11,154$ K and $\log g = 8.70$. **Top Right Panel:** Full observed spectrum with best cold model fitting, normalized at 4600Å. **Bottom Left Panel:** Best hot solution for Balmer line fitting, observed Balmer line profiles (black) and best model (red) with $T_{\text{eff}} = 19,332$ K and $\log g = 8.00$. **Bottom Right Panel:** Full observed spectrum with best hot model fitting, normalized at 4600Å.

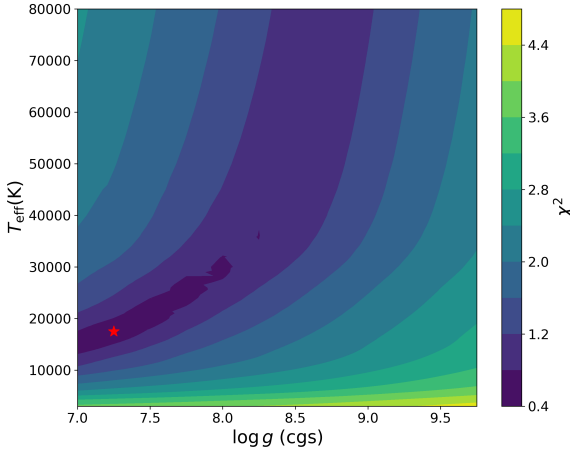


Figure 4. Contour plot of the photometric fit using the u , g , and r bands for SDSS J113907.57+511103.6. The fit is more sensitive to T_{eff} than $\log g$, with the best-matching model at $T_{\text{eff}} = 17,193$ K and $\log g = 7.49$ noted by the red star. The photometric constraints aided in selecting the preferred spectroscopic solution.

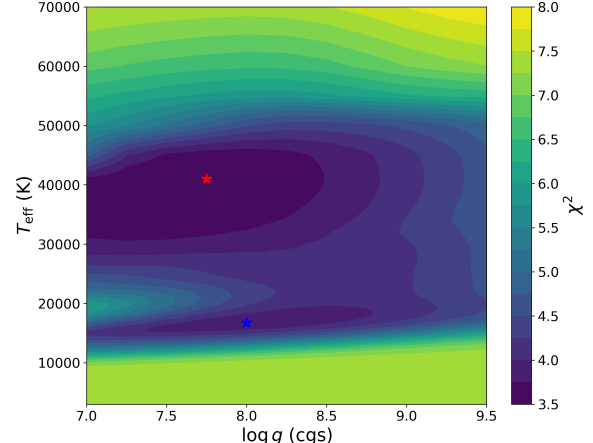


Figure 5. Contour plot of the S values computed by comparing all the pure DB models in our grid to the observed spectrum of the star SDSS J181204.26+650452.6, showing a similar degeneracy, with the red and blue stars marking the “hot” and “cold” solutions, respectively.

Table 1. SDSS names and photometry (u, g, r, i, z) and Gaia data (parallax and magnitudes in the bands G, BP, and RP) for the white dwarfs observed in the HETDEX survey with IR excess. Gaia and SDSS uncertainties are listed for each source. We verified that the majority of targets have Gaia Renormalized Unit Weight Error (RUWE), a metric assessing the goodness-of-fit of the Gaia astrometric solution, less than 1.4 and astrometric excess noise (AEN) near zero, indicating reliable astrometry. A subset of objects show elevated RUWE (up to 4.1) and AEN (up to 29 mas), likely due to unresolved companions or contamination. Reported parallaxes are adopted directly from Gaia DR3 and their uncertainties do not feature any contribution from excess noise.

Name SDSS J	u (mag)	g (mag)	r (mag)	i (mag)	z (mag)	II (mas)	G (mag)	BP (mag)	RP (mag)	Notes
011302.50-002127.4	22.064±0.14	21.188±0.04	20.969±0.04	20.119±0.03	19.491±0.05	2.125±1.061	20.575±0.009	21.184±0.259	19.711±0.104	(*)
011322.56+015105	20.595±0.06	20.184±0.02	20.406±0.03	20.692±0.05	21.345±0.28	2.252±0.667	20.299±0.007	20.244±0.080	20.167±0.132	(*)
014009.00-001243.5	21.010±0.07	20.328±0.02	19.363±0.01	18.577±0.01	18.099±0.02	0.438±0.275	19.175±0.004	20.045±0.050	18.203±0.023	(1),(3)
014152.51-005241.6	20.344±0.05	19.773±0.01	19.263±0.01	18.297±0.01	17.659±0.02	1.365±0.216	18.793±0.003	19.724±0.067	17.798±0.027	(1),(3)
015225.39-005808.6	18.411±0.02	17.890±0.01	17.695±0.01	16.980±0.01	16.255±0.01	8.733±0.101	17.292±0.003	17.866±0.013	16.428±0.008	(1),(5)
021309.19-005025.3	21.254±0.09	20.275±0.02	19.595±0.02	18.488±0.01	17.815±0.02	3.134±0.303	19.222±0.012	20.162±0.066	18.058±0.024	(1),(3)
021855.87-013543.4	19.830±0.04	18.955±0.01	18.152±0.01	17.135±0.01	16.488±0.01	1.392±0.364	17.919±0.007	18.763±18.763	16.678±0.009	(*)
021903.68-001733.9	19.383±0.02	19.250±0.01	18.920±0.01	18.107±0.01	17.502±0.01	1.513±0.193	18.516±0.004	19.227±0.039	17.644±0.019	(1),(3)
021938.57-001346.4	21.894±0.13	20.990±0.03	20.347±0.02	19.440±0.02	18.842±0.03	1.953±1.251	20.120±0.012	20.927±0.159	18.996±0.071	(1),(2)
022125.36+001710.4	21.278±0.10	20.707±0.02	20.320±0.02	19.562±0.02	19.050±0.05	—	20.364±0.021	20.7470.132	19.092±0.058	(1),(3)
110233.96+502739.9	21.734±0.12	20.933±0.03	20.314±0.02	19.264±0.02	18.551±0.03	0.478±0.411	19.826±0.005	20.673±0.100	18.695±0.029	—
113907.57+511103.6	18.788±0.02	18.691±0.01	18.758±0.01	18.307±0.01	17.800±0.02	1.605±0.593	18.980±0.004	18.759±0.016	17.878±0.014	(1),(4)
123354.89+521033.9	19.468±0.03	18.841±0.01	18.589±0.01	17.733±0.01	17.092±0.01	2.731±0.111	18.164±0.003	18.837±0.016	17.278±0.009	(*)
124158.58+544317.2	22.416±0.25	21.300±0.04	20.334±0.03	19.461±0.02	18.912±0.04	1.578±0.623	20.298±0.007	20.917±0.092	19.146±0.042	(*)
125104.96+531727.2	21.875±0.19	21.027±0.04	20.458±0.03	19.475±0.02	18.897±0.04	1.011±0.387	20.045±0.005	20.860±0.120	19.068±0.036	(*)
125351.57+510159.5	21.639±0.14	20.982±0.03	20.855±0.04	20.149±0.03	19.415±0.07	—	20.733±0.021	21.060±0.153	19.517±0.160	(*)
125656.08+540503.1	23.517±0.65	22.741±0.22	20.510±0.03	19.131±0.02	18.372±0.03	0.792±0.262	19.526±0.002	20.825±0.093	18.444±0.025	(*)
125946.43+561320.2	20.235±0.04	19.579±0.01	19.327±0.01	18.517±0.01	17.737±0.02	4.648±0.179	18.856±0.003	19.505±0.045	17.853±0.022	—
130354.53+560844.0	22.208±0.21	21.444±0.05	21.287±0.07	20.635±0.05	20.008±0.10	—	21.085±0.037	21.873±0.172	20.338±0.600	(*)
130418.62+511119.4	20.801±0.07	20.009±0.02	19.338±0.01	18.277±0.01	17.592±0.01	1.525±0.177	18.867±0.003	19.855±0.056	17.829±0.015	(*)
131315.85+535237.5	20.641±0.07	20.457±0.02	20.387±0.03	19.600±0.02	18.953±0.04	—	20.440±0.015	20.377±0.086	19.177±0.060	(*)
133237.08+510213.1	20.320±0.04	19.477±0.01	18.693±0.01	17.875±0.01	17.395±0.01	0.767±0.210	18.606±0.005	19.240±0.027	17.492±0.010	(*)
140035.96+540103.8	18.443±0.02	17.855±0.01	17.604±0.01	16.589±0.00	15.684±0.01	6.173±0.060	17.036±0.003	17.857±0.010	16.023±0.005	(*)
150959.39+511602.9	20.158±0.04	19.152±0.01	18.281±0.01	17.488±0.01	16.992±0.01	1.926±0.148	18.241±0.004	18.897±0.025	17.117±0.012	(*)
151523.32+504919.8	21.527±0.14	21.159±0.04	20.702±0.05	19.792±0.03	19.258±0.08	1.953±0.582	20.565±0.007	21.172±0.122	19.415±0.082	(*)
153343.45+535712.3	20.340±0.05	20.211±0.02	20.292±0.03	19.506±0.02	18.807±0.04	2.326±1.257	20.639±0.015	20.352±0.170	19.249±0.056	(*)
154540.48+515426.5	19.047±0.02	18.647±0.01	18.120±0.01	17.288±0.01	16.769±0.01	2.097±0.228	18.408±0.004	18.652±0.032	17.061±0.033	(*)
161051.80+503119.9	20.911±0.08	20.230±0.02	19.558±0.01	18.524±0.01	17.871±0.02	2.233±0.174	19.099±0.004	20.231±0.065	18.095±0.016	(*)
174517.73+670234.7	20.884±0.08	20.240±0.02	19.866±0.02	18.909±0.01	18.177±0.02	1.551±0.224	19.396±0.003	20.218±0.047	18.457±0.018	(*)
181204.26+650452.6	19.738±0.04	19.768±0.01	19.803±0.02	19.050±0.01	18.320±0.02	1.730±0.179	19.288±0.004	19.759±0.037	18.526±0.032	(*)

Notes: (*) Indicates targets for which the first spectroscopic observation was conducted by the HETDEX survey. (1) Targets are present in the SDSS-WDMS-Catalog (Rebassa-Mansergas et al. 2012). Targets marked with following identifiers have prior spectroscopic classification in the literature, as compiled by the Montreal White Dwarf Database (MWDD); (2) Kleinman et al. (2013). (3) Eisenstein et al. (2006); Kleinman et al. (2013). (4) Eisenstein et al. (2006); Tremblay et al. (2011); Kleinman et al. (2013). (5) Eisenstein et al. (2006); Tremblay et al. (2011); Kleinman et al. (2013); Vincent et al. (2023).

rors that affect the subsequent fitting process. Once centered, the spectral regions containing these Balmer lines were isolated to avoid introducing artifacts that could compromise the normalization process (Bergeron et al. 1992, 1995). The central wavelengths and total fitting ranges used for each Balmer line are listed in Table 2.

Following isolation, we then normalize the continuum around each line by fitting a linear function to the line wings and dividing the observed flux by this continuum fit. This procedure sets the continuum level to unity, allowing the line profile to be analyzed independently of any residual flux calibration or broadband shape in the spectrum. The lines in the DA models were isolated and normalized in the same way as the spectroscopic

data for each star, ensuring that model and observed line profiles could be compared on a consistent, continuum-normalized scale for accurate parameter fitting. This normalization procedure differs from the one used for DB white dwarfs, where the continuum is first defined by fitting a synthetic model spectrum multiplied by a high-order polynomial across a broader spectral region.

Additional processing steps before line fitting include interpolation of the model spectral fluxes onto the observed wavelength grid and convolution with a Gaussian profile to replicate instrumental resolution ($R \sim 750$) and observational conditions. These steps ensure that the spectral models are consistent with the observational

Table 2. Center of the rest wavelength (λ) and extent of the wings (λ Range) of the Balmer lines used in our spectroscopic fits for DA white dwarfs. All quantities are in Å.

Balmer Line	Rest Wavelength (λ)	λ Range
$H\beta$	4861.350 Å	± 180 Å
$H\gamma$	4340.472 Å	± 120 Å
$H\delta$	4101.734 Å	± 60 Å
$H\epsilon$	3970.075 Å	± 40 Å
$H\zeta$	3889.069 Å	± 30 Å
$H\eta$	3835.397 Å	± 20 Å

conditions, thereby enabling a more precise fitting of the models to the data.

We fit the spectroscopic lines using a least-squares approach, as described in [Zhang et al. \(1986\)](#), by minimizing the squared differences (S) between the observed spectra (I_{obs}) and the model spectra (I_{calc}):

$$S = \sum_{i=1}^n (I_{\text{obs}} - I_{\text{calc}})_i^2 \quad (1)$$

In this formulation, we assume uniform weighting (i.e., $W^{-2} = 1$) across all data points. The minimum value of S is denoted as S_0 . Following [Zhang et al. \(1986\)](#), we estimate the uncertainties (σ) in T_{eff} and $\log g$ using nearby points in the model grid.

$$\sigma^2 = \frac{d^2}{S - S_0} \quad (2)$$

Here, S_0 corresponds to the best-fit solution and S represents the next-best minimum. Following the approach of [Zhang et al. \(1986\)](#), we choose the parameter d such that the difference in T_{eff} and $\log g$ is within approximately 5% of the best-fit values. This threshold balances the need to avoid unrealistically small denominators in the error propagation when adjacent grid points have nearly identical χ^2 values while still reflecting meaningful variation in the model parameters.

In Figure 2, we show the contour plot of the comparison between all DA models in our grid with the observed spectra for the star SDSS J113907.57+511103.6. The red and blue stars indicate the two minima, which we refer to as “hot” and “cold” solutions.

This is a well-known degeneracy in Balmer line fitting, where more than one combination of effective temperature and surface gravity can produce similar Balmer line profiles. This occurs because the Balmer lines first deepen and broaden with increasing temperature, reaching maximum strength near 13,000–15,000 K due to optimal hydrogen excitation ([Rebassa-Mansergas et al. 2007](#); [Genest-Beaulieu & Bergeron 2019a,b](#)), but then

weaken at higher temperatures as hydrogen becomes increasingly ionized and fewer atoms remain at the $n = 2$ level to produce Balmer absorption. A similar degeneracy is observed in DB white dwarfs, where neutral helium lines peak in strength around 25,000 K ([Koester & Kepler 2015](#); [Genest-Beaulieu & Bergeron 2019a](#)) and weaken at both higher and lower temperatures due to changes in ionization balance. As a result, both “hot” (e.g., 20,000 K) and “cold” (e.g., 10,000 K) models can produce comparably good fits, particularly when data quality or wavelength coverage is limited.

In Figure 3, we show the comparison between the observed Balmer line profiles (left panels) and the total spectrum (right panels) for the star SDSS J113907.57+511103.6 and the best models for the “cold” solution (top panels) and the “hot” solution (bottom panels). The “cold” solution is a for model with $T_{\text{eff}} = 11,154$ K and $\log g = 8.70$ dex, while the “hot” solution model has $T_{\text{eff}} = 19,332$ K and $\log g = 8.00$ dex. Line profiles have been normalized as described in this section, while the total spectrum has been normalized at 4600 Å.

The goodness of fit for the solutions “hot” and “cold” are nearly indistinguishable by visual inspection and very similar in χ^2 ; therefore, we resort to an external determination to select our best solution.

We restricted our analysis to the u, g, and r bands due to contamination from the companion in the i and z bands. In principle, we could use the spectral energy distribution based on photometric measurements to distinguish between different temperatures. However, since our targets were selected for their infrared excess, the companion significantly contaminates the red and infrared filters, making them unreliable for this analysis ([Harris et al. 2006](#)).

To adjust for the transformation between the observed SDSS magnitudes and the AB magnitude system, we applied a correction to the u band using $u = u_{\text{SDSS}} - 0.040$ from ([Eisenstein et al. 2006](#)).

When Gaia parallax is available, we estimate distances by inverting the parallax and convert the observed apparent magnitudes in the u , g , and r bands to absolute magnitudes using the standard distance modulus equation. These absolute magnitudes are then compared with the Koester photometric models calculated for this work. In cases where no parallax is available, we instead use the color index method, comparing the observed $u - g$ and $u - r$ colors to photometric models while assuming $\log g = 8.0$. This approach follows the same methodology as for spectroscopy, applying equation 1 to fit and computing uncertainties according to equation 2.

Table 3. Spectroscopy and photometry fitting parameters for the sample. The **Spectroscopy** columns include both the hot and cold solutions for T_{eff} and $\log g$ (and $\log H/He$ for the DB star). The **Photometry** columns list the best-fit parameters from the photometric data. The **final** adopted T_{eff} and $\log g$ values, determined from the photometric analysis shown in bold.

Name SDSS J	Spectroscopy					Photometry	
	$T_{\text{eff}}(\text{Hot})\text{K}$	$\log g(\text{Hot})$	$T_{\text{eff}}(\text{Cold})\text{K}$	$\log g(\text{Cold})$	$\log H/He(\text{Hot, Cold})$	$T_{\text{eff}}\text{K}$	$\log g$
011302.50-002127.4	16,657 (546)	6.95 (0.05)	9,841 (143)	7.22 (0.023)	—	6,466	7.05
011322.56+015105.4	15,236 (237)	7.89 (0.136)	13,335 (406)	7.78 (0.101)	—	12,172	8.11
014009.00-001243.5	25,233 (1328)	7.69 (0.167)	9,781 (198)	8.79 (0.173)	—	24,953	7.10
014152.51-005241.6	19,123 (694)	8.18 (0.152)	14,430 (759)	8.55 (0.136)	—	11,411	7.23
015225.39-005808.6	29,081 (855)	7.13 (0.168)	8,833 (130)	8.49 (0.164)	—	7,008	7.35
021309.19-005025.3	20,599 (820)	7.09 (0.157)	9,629 (143)	7.98 (0.201)	—	6,314	7.06
021855.87-013543.4	26,834 (1,136)	7.10 (0.155)	8,885 (125)	8.19 (0.189)	—	15,063	7.02
021903.68-001733.9	30,930 (782)	7.97 (0.256)	9,148 (171)	9.40 (0.133)	—	12,020	7.89
021938.57-001346.4	18,277 (655)	8.08 (0.123)	13,673 (687)	8.50 (0.103)	—	6,695	7.03
022125.36+001710.4(∗)	19,501 (751)	7.38 (0.172)	9,963 (150)	8.15 (0.143)	—	6,468	8.00
110233.96+502739.9	29,829 (752)	7.58 (0.013)	8,910 (140)	8.80 (0.010)	—	17,345	7.00
113907.57+511103.6	19,332 (729)	8.00 (0.136)	11,154 (354)	8.70 (0.180)	—	17,193	7.49
123354.89+521033.9	16,253 (624)	8.10 (0.116)	15,018 (432)	8.02 (0.116)	—	9,966	7.31
124158.58+544317.2	23,979 (923)	7.97 (0.154)	9,894 (148)	8.77 (0.096)	—	6,923	7.08
125104.96+531727.2	20,779 (827)	7.01 (0.090)	9,704 (138)	7.84 (0.146)	—	9,281	7.30
125351.57+510159.5(∗)	15,053 (368)	8.48 (0.115)	13,023 (617)	8.42 (0.106)	—	6,797	8.00
125656.08+540503.1	19,166 (735)	7.12 (0.129)	9,795 (147)	7.85 (0.141)	—	7,836	7.07
125946.43+561320.2	32,833 (927)	7.26 (0.215)	8,264 (128)	8.78 (0.136)	—	6,465	7.33
130354.53+560844.0(∗)	15,100 (316)	7.21 (0.121)	14,122 (641)	7.14 (0.123)	—	6,237	8.00
130418.62+511119.4	21,166 (852)	8.08 (0.137)	14,706 (705)	8.88 (0.133)	—	9,738	7.27
131315.85+535237.5(∗)	20,012 (755)	7.76 (0.136)	10,617 (224)	8.60 (0.134)	—	8,549	8.00
133237.08+510213.1	25,015 (1,150)	7.73 (0.183)	9,618 (168)	8.67 (0.177)	—	20,997	7.01
140035.96+540103.8	19,556 (727)	7.88 (0.295)	10,983 (293)	8.55 (0.170)	—	8,216	7.34
150959.39+511602.9	22,345 (972)	7.11 (0.237)	9,377 (144)	8.08 (0.136)	—	15,063	7.04
151523.32+504919.8	28,141 (983)	7.60 (0.289)	9,223 (147)	8.76 (0.605)	—	7,075	8.12
153343.45+535712.3	21,573 (897)	8.20 (0.142)	11,045 (371)	9.10 (0.130)	—	15,215	8.52
154540.48+515426.5	21,240 (861)	7.60 (0.269)	10,463 (222)	8.65 (0.129)	—	12,705	7.43
161051.80+503119.9	26,682 (1284)	7.41 (0.162)	9,436 (152)	8.68 (0.200)	—	7,532	7.28
174517.73+670234.7	17,745 (615)	7.60 (0.146)	15,200 (200)	7.32 (0.118)	—	9,586	7.19
181204.26+650452.6(†)	40,961 (607)	7.73 (0.052)	16,828 (162)	8.02 (0.148)	-2.16 (0.052), -6.39 (0.190)	15,332	7.22

Notes: Targets marked with an asterisk (∗) lack parallax measurements. For these objects, the photometric fitting was performed using the color index method, where T_{eff} was estimated by comparing the observed $u - g$ and $u - r$ colors to Koester model predictions, assuming a fixed $\log g = 8.0$. (†) indicates the only DB white dwarf in our sample.

The assumption of $\log g = 8.0$ is motivated by the fact that the mass distribution of white dwarfs strongly peaks near $0.6 M_{\odot}$, which corresponds to $\log g \approx 8.0$ for typical white dwarf radii (e.g., Kepler et al. 2007). This provides a reasonable approximation of the photometric parameters in the absence of independent distance estimates, without introducing significant bias for the effected stars in the sample.

In Figure 4, we present the contour plot that compares the observed photometry of SDSS J113907.57+511103.6 to all models in our grid, based on fitting only the u , g ,

and r bands after converting to absolute magnitudes using Gaia parallax. Since this approach relies on only three photometric data points from the spectral energy distribution, it is significantly more sensitive to T_{eff} , than to $\log g$, which remains poorly constrained. The best matching model to the photometry and parallax in our grid corresponds to $T_{\text{eff}} = 17,193$ K and $\log g = 7.49$.

It is important to emphasize that our photometric determinations serve as an external constraint to distinguish between the “hot” and “cold” solutions derived from Balmer line fitting. For

SDSS J113907.57+511103.6, this method supports the “hot” spectroscopic solution as the best fit, resulting in $T_{\text{eff}} = 19,332$ K and $\log g = 8.00$.

We have carried out a similar analysis for all our DAs in our sample, and the results are listed in Table 3. A detailed composite-spectrum analysis of SDSS J113907.57+511103.6 using the XTGRID fitting code is presented in Appendix A, which supports the hot solution and provides additional constraints on the companion.

3.3. Fitting DB White Dwarfs

For the single DB white dwarf in our dataset, we followed a spectroscopic technique similar to that described by Bergeron et al. (2011), which differs from the fitting process used for DA white dwarfs by an additional parameter, namely the hydrogen abundance (Genest-Beaulieu & Bergeron 2019b). As DB white dwarfs have helium-dominated photospheres, the spectral analysis focuses primarily on the neutral helium absorption lines, but if present, hydrogen lines must also be considered.

We begin the fitting process by normalizing the flux of the observed spectra using our DB model grid to define the continuum. Each observed spectrum is initially fitted with a synthetic model spectrum multiplied by a high-order polynomial (typically fifth order) to account for residual flux calibration effects. The best fitting combination of model and polynomial is determined by minimizing the chi-squared between the observed and model fluxes in the wavelength range 3750–5150 Å. This polynomial scaled model provides a smoothed representation of the continuum, from which we extract flux values at predefined anchor points (e.g., 3750, 3900, 4210, 4610, 4810 and 5110, Å). We then linearly interpolate between these anchor points to define the continuum, which is used to normalize the observed spectrum by dividing by this function, effectively setting the continuum to unity.

After normalization, the observed spectrum is fitted with a pure helium DB model grid to determine T_{eff} and $\log g$, again focusing on the blue portion of the spectrum where neutral helium lines provide the strongest constraints (Genest-Beaulieu & Bergeron 2019a). As in our DA fitting procedure, all model spectra are first convolved with a Gaussian kernel to match the instrumental resolution of the observations ($R \sim 750$) prior to comparison.

In Figure 5, we show the contour plot of the S values computed by comparing all pure DB models in our grid to the observed spectrum of the star SDSS J181204.26+650452.6. As with the DAs, the DB shows a similar degeneracy, which are indicated by the

red and blue star for the “hot” and “cold” solutions, respectively.

The log H/He abundance was determined by fixing the T_{eff} and $\log g$ parameters while varying log H/He. This procedure was performed iteratively: after an initial estimate of the hydrogen abundance, we refit the spectrum to refine T_{eff} and $\log g$. We repeated this process until convergence was achieved for all three parameters, accounting for the covariance between them (Bergeron et al. 2011; Koester & Kepler 2015; Genest-Beaulieu & Bergeron 2019a).

Our estimated H β region (4681 – 5100 Å) was used instead of the typical H α region (6400 – 6800 Å) due to the spectral coverage in our sample (Rolland et al. 2018; Genest-Beaulieu & Bergeron 2019a).

To lift the degeneracy, we also used the photometric information. The results of our analysis for the only DB in our sample is in Table 3.

4. CONCLUSION AND FUTURE PROSPECTS

We have presented a spectroscopic analysis of 30 white dwarfs exhibiting infrared excess, identified within the Hobby-Eberly Telescope Dark Energy Experiment continuum catalog. The presence of IR excess in these objects, typically arising from unresolved cool stellar or sub-stellar companions, can introduce contamination that complicates spectral fitting. Using only the absorption lines in the observed spectra and the photometric measurements, we could determine T_{eff} and $\log g$ for these objects. In addition to the photospheric parameters, we confirm spectroscopically that these objects are white dwarfs. Our objects comprise a valuable list for follow-up ground-based observations to fully characterize the source of IR excess. Moreover, white dwarfs with stellar companions provide a unique opportunity to probe the effects of stellar evolution on close binary systems and the fate of stellar companions after the main sequence. These systems are ideal targets for JWST and future telescopes to resolve the IR excess or detect stellar companions.

A direct comparison of the atmospheric parameters derived from our infrared excess white dwarfs in Table 3 with DA white dwarfs in the 40 pc sample (O’Brien et al. 2024) compiled from the Montreal White Dwarf Database (Dufour et al. 2017) highlights several interesting trends. From our analysis, we find mean values of $\langle T_{\text{eff}} \rangle_{\text{IR}} = 12464$ K, $\langle \log g \rangle_{\text{IR}} = 8.26$, and $\langle M \rangle_{\text{IR}} = 0.78 M_{\odot}$. In contrast, the corresponding means for the local (40 pc) DA population are $\langle T_{\text{eff}} \rangle_{40\text{pc}} = 8650$ K, $\langle \log g \rangle_{40\text{pc}} = 8.08$, and $\langle M \rangle_{40\text{pc}} = 0.65 M_{\odot}$. This indicates that the infrared-excess sample, on average, has significantly higher effective temperatures and surface

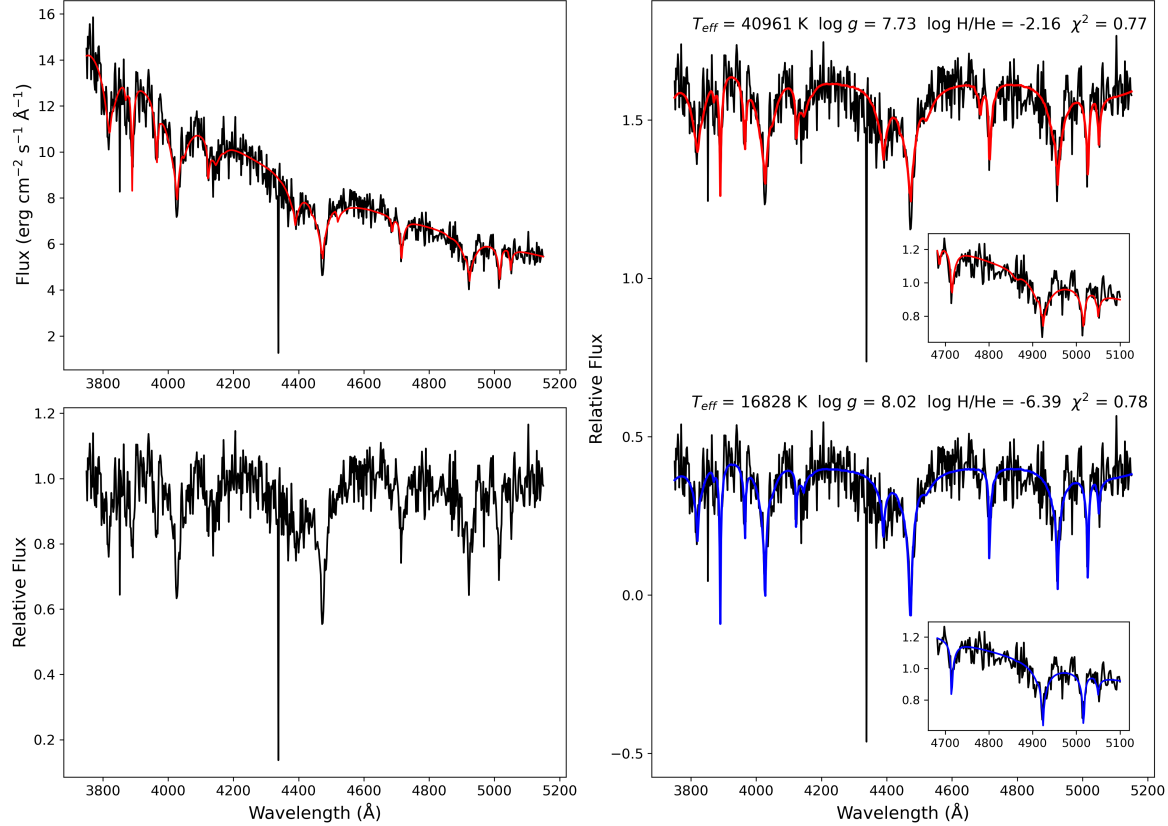


Figure 6. Example of our DB white dwarf fitting procedure for SDSS J181204.26+650452.6, the only DB white dwarf in our dataset. **Top Left Panel:** The observed spectrum (black) with the flux calibration function is applied to determine the continuum. The red line represents the scaled model used for this calibration step. **Bottom Left Panel:** The normalized spectrum after dividing by the continuum function, showing the absorption features in relative flux units. **Right Panel:** The best-fit models overlaid on the observed spectrum, with the “hot” solution ($T_{\text{eff}} = 40961$ K, $\log g = 7.73$, $\log \text{H/He} = -2.16$, $\chi^2 = 0.77$) shown in red and the “cold” ($T_{\text{eff}} = 16828$ K, $\log g = 8.02$, $\log \text{H/He} = -6.39$, $\chi^2 = 0.78$) in blue. The models are offset for clarity, and the inset highlights the H β region (4681–5100 Å) used for determining the hydrogen abundance.

gravities thus larger masses compared to the broader nearby DA white dwarf sample, as shown in Figure 7. These differences might suggest younger cooling ages or higher-mass progenitor systems for the IR-excess white dwarfs, possibly indicating more recent or active planetary system interactions. Additionally, we note that 9 of our targets have masses above $1 M_{\odot}$ (excluding the single DB in our sample). However, these high masses should be interpreted cautiously since, as discussed in Rebassa-Mansergas et al. (2019), such objects could potentially be non-DA white dwarfs, leading to significant uncertainties in their derived atmospheric parameters and masses.

5. ACKNOWLEDGMENTS

NSF research grant number 2108737, Exploring the galaxy and its white dwarfs with the HET dark energy experiment.

HETDEX (including the WFU of the HET) is led by the University of Texas at Austin McDonald Ob-

servatory and Department of Astronomy with participation from the Ludwig-Maximilians-Universität München, Max-Planck-Institut für Extraterrestrische Physik (MPE), Leibniz-Institut für Astrophysik Potsdam (AIP), Texas A&M University, Pennsylvania State University, Institut für Astrophysik Göttingen, The University of Oxford, Max-Planck-Institut für Astrophysik (MPA), The University of Tokyo, and Missouri University of Science and Technology. In addition to Institutional support, HETDEX is funded by the National Science Foundation (grant AST-0926815), the State of Texas, the US Air Force (AFRL FA9451-04-2-0355), and generous support from private individuals and foundations.

Based on observations obtained with the Hobby-Eberly Telescope (HET), which is a joint project of the University of Texas at Austin, the Pennsylvania State University, Ludwig-Maximilians-Universität Muenchen, and Georg-August Universitaet Goettingen.

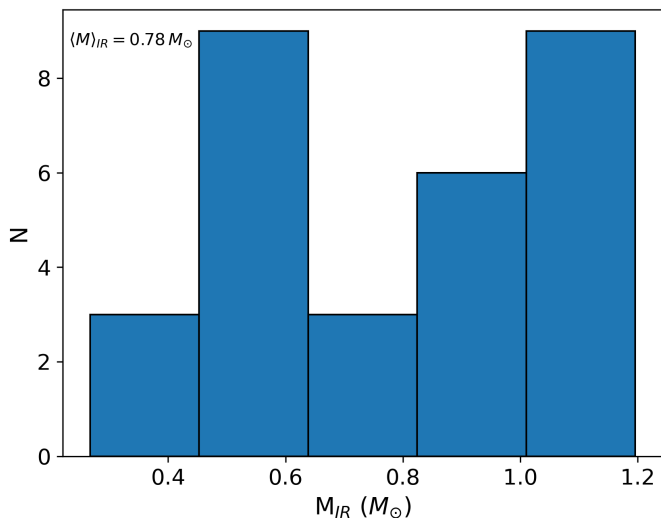


Figure 7. Mass distribution histogram for the infrared-excess DA white dwarfs in our sample. The distribution shows a mean mass of $\langle M \rangle_{IR} = 0.78 M_{\odot}$, indicating a tendency towards higher mass white dwarfs compared to the local DA population within 40 pc.

The HET is named in honor of its principal benefactors, William P. Hobby and Robert E. Eberly.

VIRUS is a joint project of the University of Texas at Austin, Leibniz-Institut fur Astrophysik Potsdam (AIP), Texas A&M University (TAMU), Max-Planck-Institut fur Extraterrestrische Physik (MPE), Ludwig-Maximilians-Universitaet Muenchen, Pennsylvania State University, Institut fur Astrophysik Goettlingen, University of Oxford, and the Max-Planck-Institut fur Astrophysik (MPA). In addition to Institutional support, VIRUS was partially funded by the National Science Foundation, the State of Texas, and generous support from private individuals and foundations.

We acknowledge the Texas Advanced Computing Center (TACC) at the University of Texas at Austin for providing computing resources that have contributed to the research results reported in this paper. URL: <http://www.tacc.utexas.edu/>. The authors thank Patrick Dufour for a fruitful discussion on the line profile fitting.

This publication makes use of data products from the Wide-field Infrared Survey Explorer, which is a joint project of the University of California, Los Angeles, and the Jet Propulsion Laboratory/California Institute of Technology, and NEOWISE, which is a project of the Jet Propulsion Laboratory/California Institute of Technology. WISE and NEOWISE are funded by the National Aeronautics and Space Administration.

P.N. acknowledges support from the Grant Agency of the Czech Republic (GAČR 22-34467S). This research has used the services of www.Astroserver.org under reference GRTO5U.

APPENDIX

A. DISENTANGLING WITH XTGRID

This appendix presents an independent spectral analysis of the composite-spectrum binary in the sample, SDSS J113907.57+511103.6. We include it here to demonstrate the viability of such an approach for future studies of composite systems.

We applied the steepest descent data-driven spectral analysis procedure XTGRID (Németh et al. 2012) to evaluate the validity of the hot and cold solutions for SDSS J113907.57+511103.6. The procedure constructs a theoretical WD+MS composite spectrum and iteratively adjusts the surface parameters of both binary components along with their flux contributions to the final spectrum. All parameters are refined to simultaneously match the detailed optical spectrum and the spectral energy distribution (SED) of the system. Various constraints can be incorporated to help break the strong degeneracies inherent in modeling composite spectra.

A key challenge in this analysis was the uncertainty in the distance to SDSS J113907.57+511103.6, as well as the unknown mass ratio and spectral types of the binary components. To address this, we assumed the mass of the DA white dwarf to be $0.6 M_{\odot}$, consistent with the peak of the DA mass distribution, and adopted its radius from the mass-radius relation. That radius allowed us to estimate the relative flux contributions to the composite spectrum, enabling a systematic search for the best-matching effective temperature (T_{eff}), surface gravity ($\log g$), and metallicity of the companion. We also assumed the system to be a bound physical binary. The adopted WD mass was then used to determine the system's distance, from which the absolute magnitude, luminosity, and radius of both components were derived. XTGRID iteratively applies these constraints in a χ^2 minimization procedure until the global minimum is reached.

The composite model consists of a DA spectrum calculated with the TLUSTY non-Local Thermodynamic Equilibrium (non-LTE) stellar atmosphere code (Hubeny & Lanz 1995, 2017), and a synthetic spectrum of an M-type main-sequence star extracted from the BOSZ (Mészáros et al. 2024) spectral library calculated with the MARCS LTE code (Gustafsson et al. 2008).

We complemented the HETDEX spectrum with an optical spectrum from the Sloan Digital Sky Survey (SDSS DR12) (Alam et al. 2015) that covers the 3800-

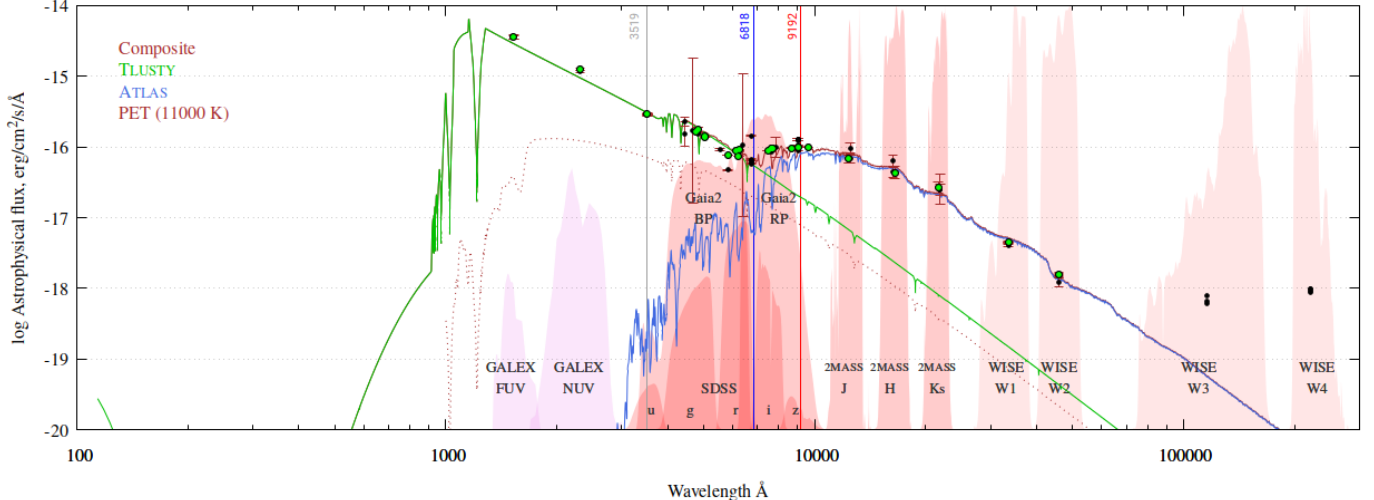


Figure A1. Spectral energy distribution (SED) of SDSS J113907.57+511103.6, showing photometric observations (black and green points with error bars) overlaid with the best-fitting composite spectral model (brown). The individual contributions from the white dwarf (TLUSTY model, green line) and the M-dwarf companion (ATLAS model, blue line) are also shown. Filter transmission curves for GALEX, SDSS, Gaia, 2MASS, and WISE bands are shaded in the background. The WISE W3 and W4 band fluxes are affected by zodiacal foreground emission. The model successfully reproduces both the ultraviolet and optical flux, as well as the infrared excess, confirming the presence of a cool main-sequence companion. The theoretical composite SED was normalized to the observed data in the SDSS *u*-band at 3519 Å. For comparison, an 11,000 K WD model is shown (PET, brown dashed line) from the synthetic spectral library of Tremblay et al. (2013).

9000 Å spectral range, and allows a good sampling of both binary members. We ran a fit with the initial constraints and started with a 19,000 K DA WD model with a fixed surface gravity ($\log g = 8.0$). We found that a 3000 K M-dwarf provides a self-consistent and nearly perfect match to both the SED and the available spectra next to an 18,350 K DA WD. Next, we repeated the analysis using the previous results as starting values and let all parameters change freely. This resulted in $T_{\text{eff}} = 18170 \pm 550$ K, and $\log g = 7.80 \pm 0.16$ for the WD, as shown in Figure A1. However, systematic errors likely supersede the statistical errors.

In contrast, repeating the procedure with an 11,000 K DA model with $\log g = 8.7$ could not reproduce the SED. Such a cool, compact, and low-luminosity WD would require a substellar companion, which is inconsistent with the observed infrared excess of the system. Even without a spectral decomposition, a cool DA WD cannot reproduce the UV slope of the SED as indicated by the GALEX FUV/NUV and SDSS *u*-band fluxes in Figure A1.

With the currently available observational data, our approach was sufficient to distinguish between the previously identified hot and cool solutions. A more comprehensive analysis will require time-resolved spectroscopy and knowledge of the dynamic mass ratio.

REFERENCES

Adams, J. J., Blanc, G. A., Hill, G. J., et al. 2011, ApJS, 192, 5, doi: [10.1088/0067-0049/192/1/5](https://doi.org/10.1088/0067-0049/192/1/5)

Alam, S., Albareti, F. D., Allende Prieto, C., et al. 2015, ApJS, 219, 12, doi: [10.1088/0067-0049/219/1/12](https://doi.org/10.1088/0067-0049/219/1/12)

Barber, S. D., Kilic, M., Brown, W. R., & Gianninas, A. 2014, ApJ, 786, 77, doi: [10.1088/0004-637X/786/2/77](https://doi.org/10.1088/0004-637X/786/2/77)

Bergeron, P., Saffer, R. A., & Liebert, J. 1992, ApJ, 394, 228, doi: [10.1086/171575](https://doi.org/10.1086/171575)

Bergeron, P., Wesemael, F., Lamontagne, R., et al. 1995, ApJ, 449, 258, doi: [10.1086/176053](https://doi.org/10.1086/176053)

Bergeron, P., Wesemael, F., Dufour, P., et al. 2011, ApJ, 737, 28, doi: [10.1088/0004-637X/737/1/28](https://doi.org/10.1088/0004-637X/737/1/28)

Cunningham, T., Wheatley, P. J., Tremblay, P.-E., et al. 2022, Nature, 602, 219, doi: [10.1038/s41586-021-04300-w](https://doi.org/10.1038/s41586-021-04300-w)

Debes, J. H., Hoard, D. W., Kilic, M., et al. 2011, ApJ, 729, 4, doi: [10.1088/0004-637X/729/1/4](https://doi.org/10.1088/0004-637X/729/1/4)

Dennihy, E., Farihi, J., Gentile Fusillo, N. P., & Debes, J. H. 2020, ApJ, 891, 97, doi: [10.3847/1538-4357/ab7249](https://doi.org/10.3847/1538-4357/ab7249)

Dufour, P., Blouin, S., Coutu, S., et al. 2017, in Astronomical Society of the Pacific Conference Series, Vol. 509, 20th European White Dwarf Workshop, ed. P. E. Tremblay, B. Gaensicke, & T. Marsh, 3, doi: [10.48550/arXiv.1610.00986](https://doi.org/10.48550/arXiv.1610.00986)

Eisenhardt, P. R. M., Marocco, F., Fowler, J. W., et al. 2020, *ApJS*, 247, 69, doi: [10.3847/1538-4365/ab7f2a](https://doi.org/10.3847/1538-4365/ab7f2a)

Eisenstein, D. J., Liebert, J., Koester, D., et al. 2006, *AJ*, 132, 676, doi: [10.1086/504424](https://doi.org/10.1086/504424)

Farihi, J., Su, K. Y. L., Melis, C., et al. 2025, *ApJL*, 981, L5, doi: [10.3847/2041-8213/adae88](https://doi.org/10.3847/2041-8213/adae88)

Gebhardt, K., Mentuch Cooper, E., Ciardullo, R., et al. 2021, *ApJ*, 923, 217, doi: [10.3847/1538-4357/ac2e03](https://doi.org/10.3847/1538-4357/ac2e03)

Genest-Beaulieu, C., & Bergeron, P. 2019a, *ApJ*, 871, 169, doi: [10.3847/1538-4357/aafac6](https://doi.org/10.3847/1538-4357/aafac6)

—. 2019b, *ApJ*, 882, 106, doi: [10.3847/1538-4357/ab379e](https://doi.org/10.3847/1538-4357/ab379e)

Gentile Fusillo, N. P., Tremblay, P. E., Cukanovaite, E., et al. 2021, *MNRAS*, 508, 3877, doi: [10.1093/mnras/stab2672](https://doi.org/10.1093/mnras/stab2672)

Gianninas, A., Bergeron, P., & Ruiz, M. T. 2011, *ApJ*, 743, 138, doi: [10.1088/0004-637X/743/2/138](https://doi.org/10.1088/0004-637X/743/2/138)

Girven, J., Gänsicke, B. T., Steeghs, D., & Koester, D. 2011, *MNRAS*, 417, 1210, doi: [10.1111/j.1365-2966.2011.19337.x](https://doi.org/10.1111/j.1365-2966.2011.19337.x)

Gustafsson, B., Edvardsson, B., Eriksson, K., et al. 2008, *A&A*, 486, 951, doi: [10.1051/0004-6361:200809724](https://doi.org/10.1051/0004-6361:200809724)

Harris, H. C., Munn, J. A., Kilic, M., et al. 2006, *AJ*, 131, 571, doi: [10.1086/497966](https://doi.org/10.1086/497966)

Hill, G. J., MacQueen, P. J., Palunas, P., et al. 2006, *NewAR*, 50, 378, doi: [10.1016/j.newar.2006.02.023](https://doi.org/10.1016/j.newar.2006.02.023)

Hill, G. J., Lee, H., MacQueen, P. J., et al. 2021, *AJ*, 162, 298, doi: [10.3847/1538-3881/ac2c02](https://doi.org/10.3847/1538-3881/ac2c02)

Hubeny, I., & Lanz, T. 1995, *ApJ*, 439, 875, doi: [10.1086/175226](https://doi.org/10.1086/175226)

—. 2017, arXiv e-prints, arXiv:1706.01859, doi: [10.48550/arXiv.1706.01859](https://doi.org/10.48550/arXiv.1706.01859)

Iben, Jr., I., & Tutukov, A. V. 1994, *ApJ*, 431, 264, doi: [10.1086/174484](https://doi.org/10.1086/174484)

Kepler, S. O., Castanheira, B. G., Costa, A. F. M., & Koester, D. 2006, *MNRAS*, 372, 1799, doi: [10.1111/j.1365-2966.2006.10992.x](https://doi.org/10.1111/j.1365-2966.2006.10992.x)

Kepler, S. O., Kleinman, S. J., Nitta, A., et al. 2007, *MNRAS*, 375, 1315, doi: [10.1111/j.1365-2966.2006.11388.x](https://doi.org/10.1111/j.1365-2966.2006.11388.x)

Kepler, S. O., Koester, D., Pelisoli, I., Romero, A. D., & Ourique, G. 2021, *MNRAS*, 507, 4646, doi: [10.1093/mnras/stab2411](https://doi.org/10.1093/mnras/stab2411)

—. 2024, VizieR Online Data Catalog: SDSS DR16 white dwarf and subdwarf stars (Kepler+, 2021), VizieR On-line Data Catalog: J/MNRAS/507/4646. Originally published in: 2021MNRAS.507.4646K

Kleinman, S. J., Harris, H. C., Eisenstein, D. J., et al. 2004, *ApJ*, 607, 426, doi: [10.1086/383464](https://doi.org/10.1086/383464)

Kleinman, S. J., Kepler, S. O., Koester, D., et al. 2013, *ApJS*, 204, 5, doi: [10.1088/0067-0049/204/1/5](https://doi.org/10.1088/0067-0049/204/1/5)

Koester, D. 2010, *Mem. Soc. Astron. Italiana*, 81, 921

Koester, D., & Kepler, S. O. 2015, *A&A*, 583, A86, doi: [10.1051/0004-6361/201527169](https://doi.org/10.1051/0004-6361/201527169)

—. 2019, *A&A*, 628, A102, doi: [10.1051/0004-6361/201935946](https://doi.org/10.1051/0004-6361/201935946)

Koester, D., Kepler, S. O., & Irwin, A. W. 2020, *A&A*, 635, A103, doi: [10.1051/0004-6361/202037530](https://doi.org/10.1051/0004-6361/202037530)

Lai, S., Dennihy, E., Xu, S., et al. 2021, *ApJ*, 920, 156, doi: [10.3847/1538-4357/ac1354](https://doi.org/10.3847/1538-4357/ac1354)

Liebert, J., Bergeron, P., & Holberg, J. B. 2005, *ApJS*, 156, 47, doi: [10.1086/425738](https://doi.org/10.1086/425738)

Livio, M., & Pringle, J. E. 2011, *ApJL*, 740, L18, doi: [10.1088/2041-8205/740/1/L18](https://doi.org/10.1088/2041-8205/740/1/L18)

Mainzer, A., Bauer, J., Grav, T., et al. 2011, *ApJ*, 731, 53, doi: [10.1088/0004-637X/731/1/53](https://doi.org/10.1088/0004-637X/731/1/53)

Marocco, F., Eisenhardt, P. R. M., Fowler, J. W., et al. 2021, *ApJS*, 253, 8, doi: [10.3847/1538-4365/abd805](https://doi.org/10.3847/1538-4365/abd805)

Mészáros, S., Bohlin, R., Allende Prieto, C., et al. 2024, *A&A*, 688, A197, doi: [10.1051/0004-6361/202449306](https://doi.org/10.1051/0004-6361/202449306)

Mullally, S. E., Debes, J., Cracraft, M., et al. 2024, *ApJL*, 962, L32, doi: [10.3847/2041-8213/ad2348](https://doi.org/10.3847/2041-8213/ad2348)

Németh, P., Kawka, A., & Vennes, S. 2012, *MNRAS*, 427, 2180, doi: [10.1111/j.1365-2966.2012.22009.x](https://doi.org/10.1111/j.1365-2966.2012.22009.x)

O’Brien, M. W., Tremblay, P. E., Klein, B. L., et al. 2024, *MNRAS*, 527, 8687, doi: [10.1093/mnras/stad3773](https://doi.org/10.1093/mnras/stad3773)

Reach, W. T., Kuchner, M. J., von Hippel, T., et al. 2005, *ApJL*, 635, L161, doi: [10.1086/499561](https://doi.org/10.1086/499561)

Rebassa-Mansergas, A., Gänsicke, B. T., Rodríguez-Gil, P., Schreiber, M. R., & Koester, D. 2007, *MNRAS*, 382, 1377, doi: [10.1111/j.1365-2966.2007.12288.x](https://doi.org/10.1111/j.1365-2966.2007.12288.x)

Rebassa-Mansergas, A., Nebot Gómez-Morán, A., Schreiber, M. R., et al. 2012, *MNRAS*, 419, 806, doi: [10.1111/j.1365-2966.2011.19923.x](https://doi.org/10.1111/j.1365-2966.2011.19923.x)

Rebassa-Mansergas, A., Solano, E., Xu, S., et al. 2019, *MNRAS*, 489, 3990, doi: [10.1093/mnras/stz2423](https://doi.org/10.1093/mnras/stz2423)

Rocchetto, M., Farihi, J., Gänsicke, B. T., & Bergfors, C. 2015, *MNRAS*, 449, 574, doi: [10.1093/mnras/stv282](https://doi.org/10.1093/mnras/stv282)

Rolland, B., Bergeron, P., & Fontaine, G. 2018, *ApJ*, 857, 56, doi: [10.3847/1538-4357/aab713](https://doi.org/10.3847/1538-4357/aab713)

Shulov, O. S., & Kopatskaya, E. N. 1974, *Astronomicheskij Tsirkulyar*, 810, 1

Skrutskie, M. F., Cutri, R. M., Stiening, R., et al. 2006, AJ, 131, 1163, doi: [10.1086/498708](https://doi.org/10.1086/498708)

Tremblay, P. E., & Bergeron, P. 2007, ApJ, 657, 1013, doi: [10.1086/511330](https://doi.org/10.1086/511330)

Tremblay, P. E., Bergeron, P., & Gianninas, A. 2011, ApJ, 730, 128, doi: [10.1088/0004-637X/730/2/128](https://doi.org/10.1088/0004-637X/730/2/128)

Tremblay, P. E., Ludwig, H. G., Steffen, M., & Freytag, B. 2013, A&A, 559, A104, doi: [10.1051/0004-6361/201322318](https://doi.org/10.1051/0004-6361/201322318)

Vincent, O., Bergeron, P., & Dufour, P. 2023, MNRAS, 521, 760, doi: [10.1093/mnras/stad580](https://doi.org/10.1093/mnras/stad580)

Wilson, T. G., Farihi, J., Gänsicke, B. T., & Swan, A. 2019, MNRAS, 487, 133, doi: [10.1093/mnras/stz1050](https://doi.org/10.1093/mnras/stz1050)

Winget, D. E., & Kepler, S. O. 2008, ARA&A, 46, 157, doi: [10.1146/annurev.astro.46.060407.145250](https://doi.org/10.1146/annurev.astro.46.060407.145250)

Woosley, S. E., & Heger, A. 2015, ApJ, 810, 34, doi: [10.1088/0004-637X/810/1/34](https://doi.org/10.1088/0004-637X/810/1/34)

Wright, E. L., Eisenhardt, P. R. M., Mainzer, A. K., et al. 2010, AJ, 140, 1868, doi: [10.1088/0004-6256/140/6/1868](https://doi.org/10.1088/0004-6256/140/6/1868)

Xu, S., Lai, S., & Dennihy, E. 2020, ApJ, 902, 127, doi: [10.3847/1538-4357/abb3fc](https://doi.org/10.3847/1538-4357/abb3fc)

Zeimann, G. R., Debski, M. H., Schneider, D. P., et al. 2024, ApJ, 966, 14, doi: [10.3847/1538-4357/ad35b8](https://doi.org/10.3847/1538-4357/ad35b8)

Zhang, E. H., Robinson, E. L., & Nather, R. E. 1986, ApJ, 305, 740, doi: [10.1086/164288](https://doi.org/10.1086/164288)

Zuckerman, B., & Becklin, E. E. 1987, Nature, 330, 138, doi: [10.1038/330138a0](https://doi.org/10.1038/330138a0)